Design and calibration of a closed loop tip-tilt control for a pyramid-Shack-Hartmann hybrid wave-front sensor

Jean, Madison, Knight, Justin, Guthery, Charlotte, Hart, Michael, Kim, Daewook

SPIE.

Design and calibration of a closed loop tip-tilt control for a pyramid-Shack-Hartmann hybrid wave-front sensor

Madison Jean*[a], Justin M. Knight[a] ,Charlotte Guthery[a], Michael Hart[a], Daewook Kim[a]

[a]James C. Wyant College of Optical Sciences, University of Arizona, 1630 E. University Blvd., Tucson, AZ, 85721, USA

ABSTRACT

The Hybrid Wave-front Sensor (HyWFS) has previously been developed as a combination of a Pyramid Wave-front Sensor (PyWFS) and a Shack-Hartmann Wave-front Sensor (SHWFS) to capture the desirable properties of each when operated with an unresolved guide beacon. A pyramid prism placed at a focus divides the beacon light into four beams. At a reimaged pupil, a lenslet array creates four separate spot patterns on a detector. The measured intensities may be analyzed both in the manner of a PyWFS and a SHWFS, generating two approximations of the wave front that together achieve the high sensitivity of the PyWFS and the high dynamic range of the SHWFS. Given its inherent sensitivity, calibrating the HyWFS is challenged by the effects of local vibrations and air currents in the laboratory. To overcome this problem, a prototype HyWFS has been built that features a closed loop tip-tilt control sub-system. The design includes additional pupil planes, a Fast Steering Mirror (FSM), and a tip-tilt sensor. The prototype HyWFS will be calibrated with low-order Zernike polynomials at a variety of amplitudes to confirm the sensor's sensitivity, dynamic range, and the effectiveness of the tip-tilt control loop. The effect of the tip-tilt loop will be quantified by comparing calibration qualities while the loop is active and inactive. The residual wave-front error is anticipated to decrease with active tip-tilt control in both the PyWFS mode and the SHWFS mode. With improved accuracy, the HyWFS is another step closer to on sky operation in a closed-loop adaptive optics system.

Keywords: Adaptive optics, Atmospheric turbulence, Wave-front sensing, Hybrid wave-front sensor, Tip-tilt control, Shack-Hartmann wave-front sensor, Pyramid wave-front sensor

1. INTRODUCTION

1.1 Wave-front Sensing and Adaptive Optics

The ease with which the amplitude and phase of electromagnetic radiation can be directly detected is strongly dependent on wavelength. For example, radio wave detection is often achieved by mixing an incoming frequency with another frequency of near equal value that is generated by a local oscillator. This creates heterodyne frequencies, and with simple signal processing yields the phase and amplitude of the incoming signal[1]. If this same principle were applied in the detection of light in the visible and infrared (IR) spectrum, at wavelengths orders of magnitude smaller, the bandwidth required of the corresponding local oscillator i.e., a laser, and the longest permissible integration time of the signal capture will also be orders of magnitude smaller. Thus, heterodyne detection of the phase at these wavelengths places a very severe lower limit on the in-band brightness of the source. These challenges have given rise to the development of optical wave-front sensors.

Current optical wave-front sensors typically employ some method of partitioning or redirecting sections of a pupil of collected light to obtain irradiances at different locations in the pupil. According to the manner of pupil manipulation, the irradiances are analyzed to approximate their relationship to the incoming wave-front's electric field phase. For example, the estimated relationship could be local wave-front gradients or normalized intensity differences. A collection of these values, represented by a matrix, can be integrated or combined to reconstruct of the full shape of the wave-front. Wave-front sensors are an essential component in Adaptive Optics (AO) systems for aberration correction. In an AO system, the incoming wave-front is approximated by the wave-front sensor. Then, the reconstruction is used to inform the movement of a Deformable Mirror (DM) that counteracts the detected aberrations[2]. The process is repeated continuously to converge to a near diffraction limited image, either in closed or open loop depending on the application.

*jean.madison22@gmail.com

In general, there are three attributes to consider when choosing a wave-front sensor for use in an AO system. These are linearity, sensitivity, and dynamic range. Sensitivity is often described by the sensor's ability to detect wave-front difference or slopes at specific spatial frequencies for a specific amount of collected light. Dynamic range is generally described as the difference or ratio of the greatest to the smallest errors the sensor can detect[3]. Lastly, linearity refers to the signal response of the sensor. The ideal wave-front sensor makes efficient use of incoming photons, and supports fast wave-front estimations with the lowest noise propagation. For wave-front sensors in current use, high sensitivity is generally achieved at the expense of dynamic range and vice versa.

1.2 Hybrid Wavefront Sensors

The development of some standard wave-front sensors have reached their respective limits regarding sensitivity and dynamic range. To push the boundaries of wave-front sensing and avoid costly trade-offs, researchers have begun combining sensors, or their operating principles, to work in tandem as hybrid wave-front sensors. For example, hybrid wave-front sensors consisting of varying combinations of curvature, gradient, Shack-Hartmann (SHWFS), interferometric, and holographic modal wave-front sensors have previously been proposed and tested with promising results. A hybrid curvature-gradient wave-front sensor has demonstrated in testing that there does exist a hybrid system and membrane mirror combination that yields a diagonal, or linear, response matrix[4]. Another hybrid, a Shack-Hartmann-interferometric wave-front sensor has been shown to yield better performance, in terms of Strehl ratio, in open loop than either respective wave-front sensor individually[5]. Additionally, a low resolution SHWFS-holographic modal wave-front sensor hybrid in on-sky, closed-loop simulation allowed for an increase the dynamic range of the holographic modal wave-front sensor[6]. Further developing their hybrid wavefront sensor and the previously mentioned curvature-gradient wave-front sensor, Dong et al. then combined a curvature sensor and holographic modal wavefront sensor to achieve a similar result: clever customization of a hologram allows for an increase in both sensitivity and dynamic range of the holographic modal wave-front sensor[7].

Most recently, the Adaptive Optics Lab at the University of Arizona's Wyant College of Optical Sciences has theorized and built a prototype Pyramid-Shack-Hartmann Hybrid wave-front sensor[8,9] (HyWFS). The HyWFS generates two wave-front estimations, one calculated in a Pyramid wave-front sensor (PyWFS) mode and one in a SHWFS mode. Which reconstruction to apply depends on the magnitude of the input aberrations. The PyWFS is more sensitive, and therefore better performing, than the SHWFS at small aberration amplitudes, while the SHWFS allows for reliable reconstruction of larger amplitude aberrations, once the PyWFS response is saturated. This specific combination of wave-front sensors has not been previously explored and may be of great value to the AO community given their complimentary sensitivities and dynamic ranges and ability to seamlessly switch between reconstruction modes. In addition to being a promising combination for a HyWFS, the SHWFS and the PyWFS are already widely used, making development relatively accessible.

1.3 HyWFS with Closed Tip-Tilt Control Loop

The HyWFS achieves the integration of a PyWFS and a SHWFS by placing a lenslet array at the collimated image of the four pupils created by a focused spot incident on the tip of a pyramid prism. The changing shape of the focused spot on the pyramid creates intensity variations in the resulting pupils. Each pupil is sampled by the lenslet array, creating a pattern of focused spots at the focal plane of the lenslet array, which are captured on a CCD detector. With proper pixel binning and image processing, the system yields two approximations of the wave-front reconstruction, simultaneously. For calibration and, ultimately, closed-loop operation as part of an AO system, the HyWFS includes a continuous membrane DM. A schematic of the HyWFS and its test bench can be seen in Figure 1.

Due to the inherent sensitivity of the PyWFS and random motion of the diffraction-limited spot on the pyramid tip, calibration of the HyWFS in the laboratory setting is challenging. To address the challenge in calibration, a closed tip-tilt control loop (TTL) has been developed and included in the HyWFS prototype. The TTL uses a Fast Steering Mirror (FSM) to continuously adjust tip and tilt in an effort to overcome the effects of local air currents or temperature gradients in the lab. The prototype now includes the FSM and a tip-tilt sensor, comprising the TTL, and a designated location to insert a phase plate. The TTL was calibrated to determine the relationship between focus spot movement and applied voltage to the FSM. This relationship is then utilized in the control loop, which when active, demonstrates a decrease in the random lateral motion of the focused spot on the tip-tilt sensor. The addition of the TTL to the HyWFS brings the wave-front

sensor another step closer to closed loop, on sky operation, as well as serves as an example tool for mitigating environmental disturbances in a laboratory setting.
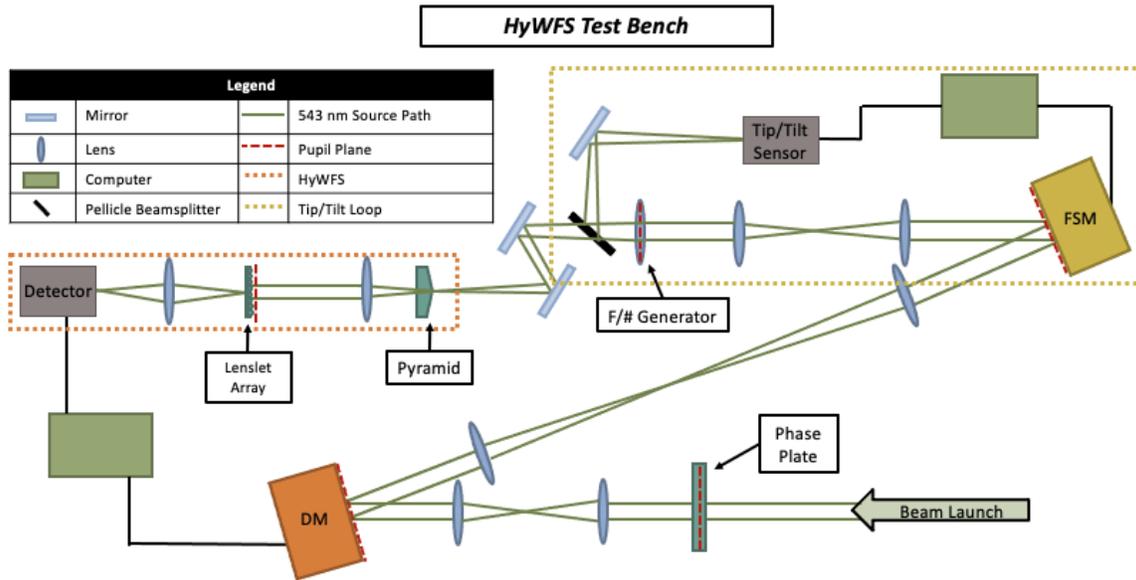

Figure 1. Schematic diagram of the HyWFS test bench configuration and beam path. The HyWFS is marked as the red-botted box and the Tip-Tilt Loop is shown in the yellow-dotted box.

2. OPTICAL DESIGN OF HYWFS TEST BENCH

2.1 HyWFS Design

The HyWFS prototype is comprised of a high f/# input beam that is focused on two crossed roof prisms rather than a monolithic pyramidal prism, followed by a collimating lens, a lenslet array, a relay lens, and a detector[10,11]. From left to right, a simplified representation of this HyWFS subsystem is shown below in Figure 2.
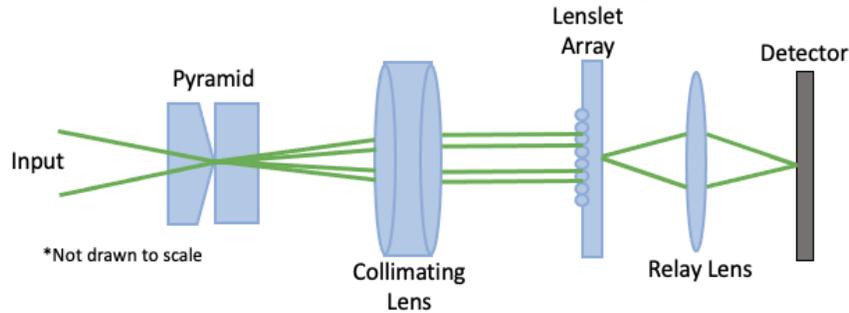

Figure 2. Simplified optical schematic of the HyWFS consisting of the pyramid prisms followed by the collimating lens to create the quadrant pupil plane at the lenslet array. The focused array of spots is imaged on the detector through the relay imaging optics.

More specifically, well focused incoming light, where the central lobe of the focused spot is centered on the four quadrants of the pyramid's tip, is divided into four pupils. These four pupils are identical to one another if the incoming light is unaberrated. The pupils are then collimated onto an array of microlenses that further split and an focus the light through subaperture. To accommodate for mechanical clearances, a relay lens reimages the array of spots onto the detector, a FLIR Grasshopper 3 sCMOS camera. The size of the active and further buffered region of the camera limits the full extent of the resulting spot pattern output by the HyWFS to no greater than 1160 pixels, or 6.8 mm. Determined through iterative paraxial raytrace modeling, the final specifications of the HyWFS's optical design are as follows in Table 1.

Table 1. Specification of the HyWFS's optical design

Specification	Value
Input Beam F/#	83.4
Roof Prism Angle	0.748°
Focal Length, Collimating Triplet	125 mm
Number of Lenslets	361, 19 x 19
Diameter, One Lenslet	188 μm
Focal Length, One Lenslet	5.2 mm
Focused Spot Spacing	32 pixels
Detector Pixel Pitch	5.86 μm

This design yields eight samples across each pupil generated by the pyramid. The geometry was confirmed with a non-sequential ray trace of the model in Zemax OpticStudio. Figure 3 shows the HyWFS as a bench top experiment. Figure 4 is an example of the output image of the HyWFS. The lenslet array creates a pattern of focused spots at the detector with varying intensities created by the pyramid. Diffraction from the edges of the pyramid scatters some of the light outside the geometric pupil boundaries. The images are binned to perform PyWFS mode calculations and cropped by pupil and summed to perform SHWFS calculations.
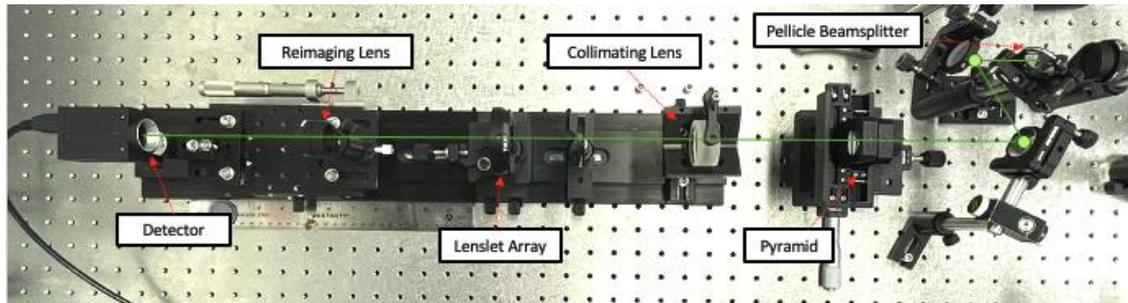

Figure 3. Labeled photograph of the HyWFS on the test bench, this corresponds to the components in the red-dotted box in Figure 1. The nominal beam propagation axis is shown as a green ray.
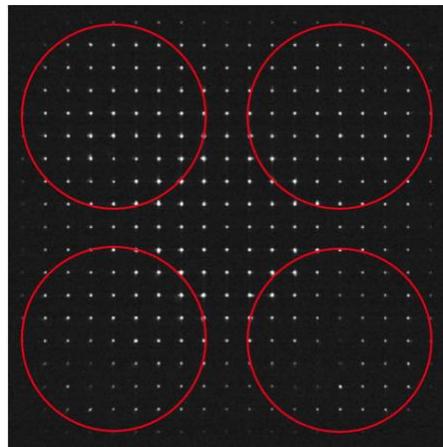

Figure 4. Measured irradiance image of HyWFS output at the final detector plane displaying the quadrant image of the focused spot array

2.2 Bench and TTL Design

The HyWFS is at the output of an adaptive optics system that includes the DM and the FSM, located at pupil planes. These components allow for characterization of the wave-front sensor's response to known aberrations. The combination of the

two creates the test bench, represented by the diagram seen previously in Figure 1. The DM is used to apply mid to low order Zernike polynomials, and the FSM, as part of the TTL, is used to minimize the tip and tilt effects induced by the lab environment. The test bench's DM was manufactured by Boston Micromachines Corporation (BMC) and has 140 electrostatic actuators. Produced by Optics In Motion (OIM), the FSM is a protected Aluminum coated 2 inch mirror, with a full angular range of 3°, ±1.5°, and capable of approximately 1 µrad steps. It is driven in tipped and tilted by magnet voice coil actuators along two axes in a push-pull configuration

Three afocal pupil relays accommodate pupil locations at a plane just after the system's beam launch, at the DM's surface, at the FSM's surface, and at the entrance pupil of the f/# generating lens of the HyWFS; each relay is referred to in Figure 1. To direct light to the TTL, a pellicle beamsplitter is placed in a converging beam. This is done to have the split beam's focused spot on the tip-tilt sensor as analogous to the focused spot on the pyramid as possible. Further, a pellicle beamsplitter was chosen over a cube beamsplitter to minimize the amount of optical path introduced while creating the TTL arm. A simplified diagram of the TTL as well an image of the full system can be seen in Figures 5 and 6 below.
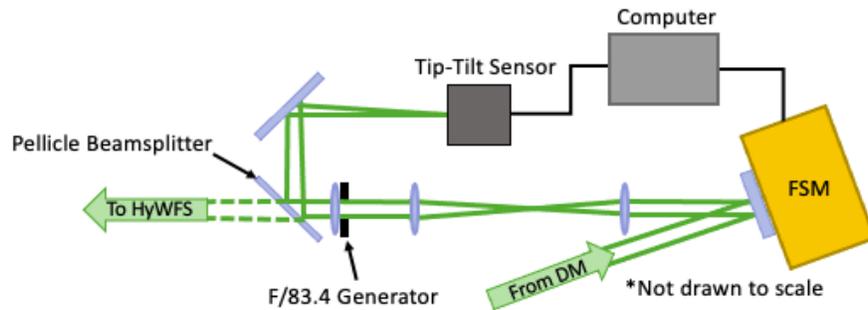

Figure 5. Schematic diagram of the TTL with the beam path shown at green rays. This corresponds to the components in the yellow-dotted box in Figure 1.
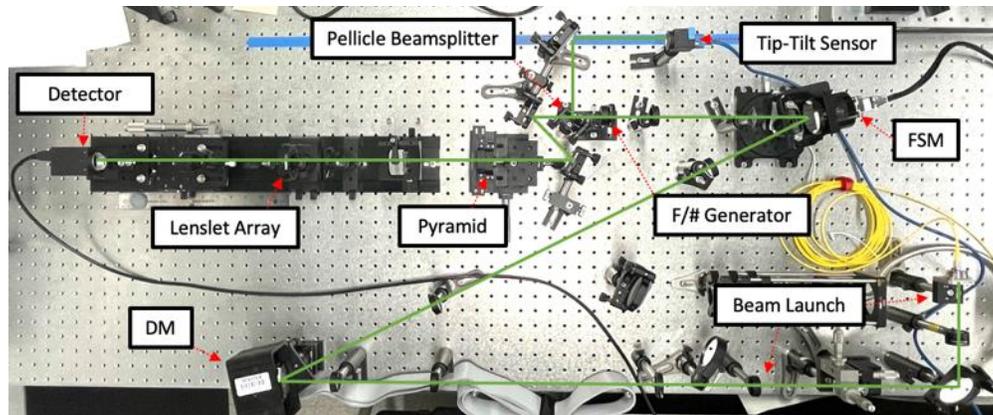

Figure 6. Labeled photograph of the actual HyWFS test bench configuration with the green ray representing a nominal beam propagation axis.

3. CALIBRATION AND TESTING OF TTL

3.1 Calibration Method

To calibrate the movement of the focused spot on the tip-tilt sensor to applied voltage at the FSM, an iterative function sends a voltage command to the FSM, captures an image of the sensor, calculates the centroid, stores that position, and repeats the process for a range of voltage values. First though, a method for image reduction, or confirmation that it may forgone, must be explored.

Three methods of image reduction, which occurs before the centroid calculation is completed on each focused spot image, are considered: none, or a raw image, binarizing at half the maximum pixel value, and thresholding in addition to background subtraction. In the case a raw image is used, it is passed directly to a function that calculates the geometric center of the focused spot on the detector in pixels, with respect to center pixel. In the case that the raw image is thresholded at half the maximum pixel value, the image passed to the centroid function is a binary image, where all pixels in the raw image with a value greater than half the maximum pixel value are equal to 1 and all pixels less than that value are equal to 0. Lastly, in the case the raw image is dark subtracted and thresholded, the image that is passed to the centroid calculation is created by subtracting a dark image of the detector from a raw image, pixel by pixel, then thresholding according to the median dark pixel value, setting all pixels less than this value equal to 0. The spot movement response to FSM tilt was calibrated using each image reduction method. In the following figures are plots of the centroid, or focused spot, movement in pixels as a function of command in μV applied to the FSM. A linear fit of the plots below, will yield a pixel shift per μV calibration factor that is then used for active tip-tilt correction.
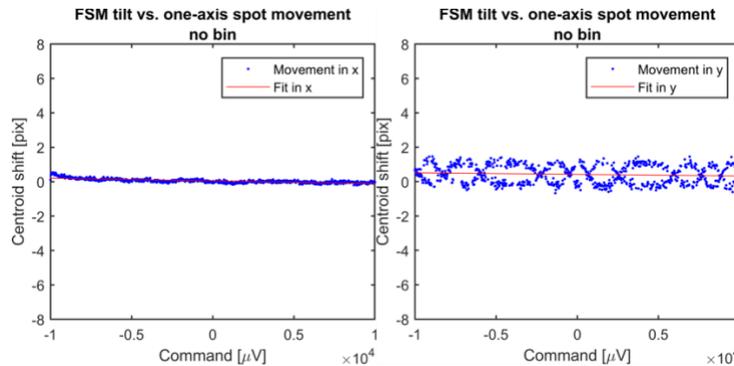

Figure 7. Spot movement, expressed as centroid shift in pixels, vs applied FSM command in μV when raw images are used
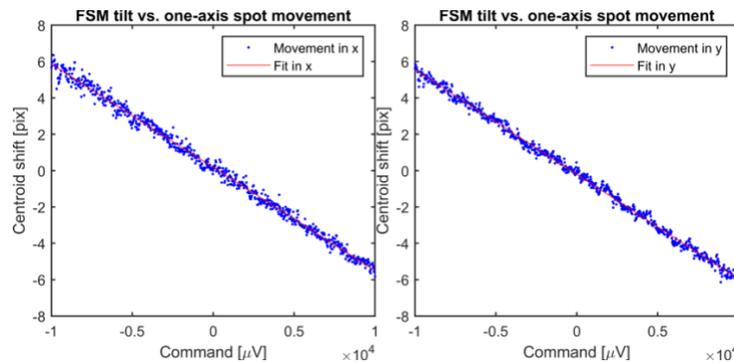

Figure 8. Spot movement, expressed as centroid shift in pixels, vs applied FSM command in μV when binarized images are used
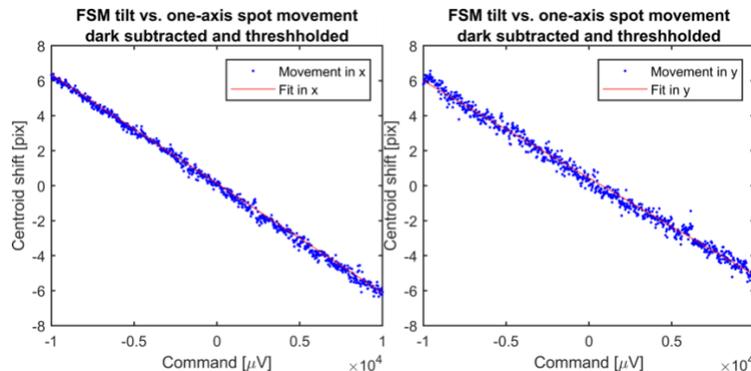

Figure 9. Spot movement, expressed as centroid shift in pixels, vs applied FSM command in μV when dark subtracted and thresholded images are used

The plots in Figure 7 clearly suggest that some form of image reduction is necessary for obtaining a reliable calibration factor for the TTL. The variation in pixel shifts and trend towards an average of none, or a constant shift, despite movement of the FSM, indicates a bias in centroid estimates from low-information pixels when using the entire detector pixel array. Therefore, the effectiveness of binarizing and dark subtracting and thresholding during correction will be compared in testing.

3.2 Testing Method and Operation

To test the correction quality yielded by both relevant methods of image reduction, the TTL is activated for a period of time and compared to the spot movement on the tip-tilt sensor, without correction and calculated with the same image reduction method, over the same period of time. The comparison is with respect to the variance of the collection of centroid values calculated from the captured images as well as determined visually with a 2-dimensional plot of centroid locations.

For correction, the initial x and y-direction commands for the FSM are set to 0. When the correction loop is initiated, one frame is captured from the detector and reduced according to the chosen method. Then the centroid, with respect to the center of the detector, is calculated and the returned coordinate values, with the calibration factor, determine the correction command to be added to the FSM. A correction command is expressed by Equation 1.

$$V_{x,y_n} = V_{x,y_{n-1}} + \left(0.5 * \left(C_{x,y} * CAL_{x,y}\right)\right)$$

(1)

Vx,y is either the x or y-direction voltage in μV, Cx,y is either the x or y coordinate of the most recently calculated centroid, and $CALx,y$ is the respective x or y-direction calibration factor. The new voltage command, Vn, is the addition of the most recent voltage command, $Vn-1$, and one half of the centroid Cx,y coordinate scaled by $CALx,y$. As the voltage commands can be thought of as position commands, the Cx,y, $CALx,y$ product is multiplied by 0.5 and then added to the previous command. Adding the full Cx,y, $CALx,y$ product to the previous command could be the optimal gain value, as the TTL is a type 1 servo loop, but a gain factor of 0.5 has been arbitrarily chosen here.

4. TTL PERFORMANCE

4.1 Results

The following table and figures contain numerical and visual representations of the residual spot movement variances during correction loop operation with both image reduction methods.

Table 2. Statistics of correction performance when using both image reduction methods, binarization and dark subtracting and thresholding

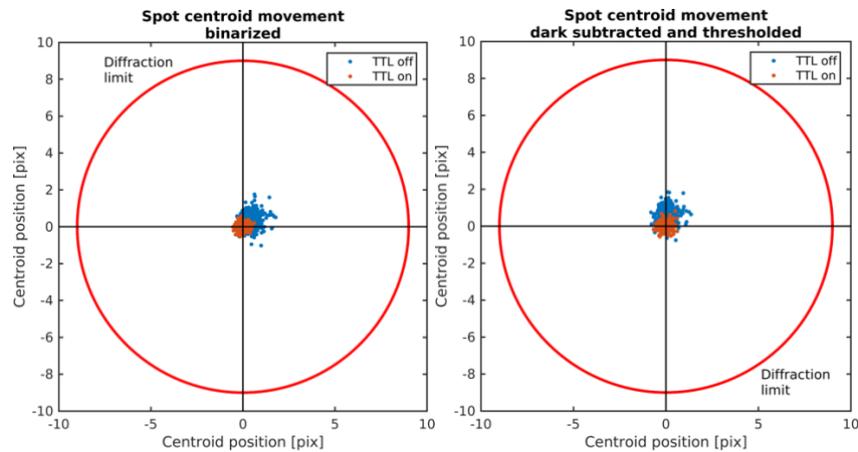|	Binarization		Dark Sub + Thresh	
Statistic	TTL OFF	TTL ON	TTL OFF	TTL ON
Variance (pixels^2)	0.01	0.030	0.093	0.041
Standard Deviation (pixels)	0.316	0.173	0.305	0.202
Percent Difference		69.96%		56.34%

Figure 10. (left) Movements of focused spots, both with the TTL on and off, represented by 2D plot of centroid locations using binarization method. (right) Movements of focused spots, both with the TTL on and off, represented by 2D plot of centroid locations using dark subtraction and thresholding method.

4.2 Discussion

As mentioned in section 3.1, calculating the spot centroids with raw images maintains many low-information pixels in the images, which prevents reliable centroid location. This could be mitigated by decreasing the image size to a smaller region of interest around the focused spot or as confirmed by Figure 8, binarizing the images. Binarizing the images at a threshold of half the maximum pixel value eliminates any possible contribution from these pixels because a threshold is being used to set low-information pixels to no-information pixels. However, the accuracy of the centroid estimate may be affected as the 'edges' of the Airy pattern are weighted the same as the center. As for the method of thresholding and dark subtraction, it also eliminates the effect of low-information pixels but in addition, may allow centroids to be determined more accurately as the weights associated with varying positions across the Airy pattern maintain their natural relative values. Further, this method, if used with image capture during active correction as well, also provides the advantage of robustness when non-radially symmetric aberrations are applied by the DM or induced on sky.

These observations and predictions are supported by the plots seen in Figure 10. By calibrating the detector response and operating the TTL with images that have been binarized, the percent decrease in residual spot movement is about 70%, while with images that are dark subtracted and thresholded, the percent decrease is about 56%. Evidently, both image reduction methods deliver a similar performance. In this setting, binarization outperforms dark subtraction and thresholding, though it is worth exploring the effects of using smaller image window on the detector and dark subtraction and thresholding when working with an aberrated beam. Further developing the command equation and fine tuning proportional, integral, and derivative gains may also bring the TTL to its full potential. This test confirms the need for image reduction when calculating centroid locations but suggests that continued consideration of optimal parameters of either method, as well as the impact of the TTL on HyWFS itself, are prerequisites of a fully optimized test bench or instrument.

4.3 Calibration of HyWFS with TTL

The next step in characterizing and fine tuning the HyWFS is to introduce the TTL into its calibration. The HyWFS will be calibrated by cataloging its response to a known library of Zernike polynomial shapes that are applied to the DM. This process yields a reconstruction matrix that will allow for an unknown combination of aberrations to be approximated by a collection of Zernike polynomials that are applied to the DM for compensation. With the help of the TTL, calibration of the HyWFS is expected to be more precise than without. This will be determined by calibrating the HyWFS while the TTL is active. The TTL can run autonomously to move the focused spot to a set pixel on the tip-tilt sensor corresponding to the pyramid tip as various shapes are applied to the DM, but this eliminates any tip-tilt effects created by the DM. To avoid this when calibrating the HyWFS, the set pixel must be changed while simultaneously monitoring the commands applied to the FSM to calculate the mean change.

5. CONCLUSIONS

The HyWFS has been theorized, developed, and prototyped as a combination of a PyWFS and SHWFS. This wave-front sensor allows for two different estimations of wave-front error from a single image: one more sensitive to aberrations at small spatial scales when generated in PyWFS mode, and another with a greater dynamic range when generated in SHWFS mode. Together they create a wave-front sensor that is both sensitive and highly dynamic, while only requiring one non-partitioned detector. Through previous testing, it was determined that the HyWFS is so sensitive that local air currents in the laboratory setting are detrimental to the accuracy to which the wave-front sensor can be calibrated to known aberrations. This problem will to be mitigated by simultaneous operation of the TTL. The TTL iteratively captures an image of a focused spot that is analogous to the spot that is focused on the tip of the pyramid, calculates the spot's position on the detector, and adjusts the FSM accordingly to direct it back to the center of the detector.

Through calibration and testing of the TTL, it is poised to help the HyWFS achieve operation on-sky with an unresolved beacon, as part of an AO system. Depending on the method of image reduction used prior to calculating spot centroids, the reduction in residual spot movement from inactive to active tip-tilt correction is at least 56% or possibly as great as 70%. These results leave room for further exploration into the HyWFS's principle and operation as well as suitable image reduction and correction tuning for the TTL when they operate together.

REFERENCES

[1] Electric Club, P. E. journal., [Electric Journal], Pittsburg (1904).
[2] van Dam, M., Clare, R. and Observatory, W. M. K., "Wavefront reconstruction for adaptive optics," 54.
[3] Adamy, D., "Receiver Sensitivity and Dynamic Range," Practical Communication Theory, 93–108 (2014).
[4] Paterson, C. and Dainty, J. C., "Hybrid curvature and gradient wave-front sensor," Optics Letters **25**(23), 1687 (2000).
[5] Ellis, T. R., "Shack-Hartmann and Interferometric Hybrid Wavefront Sensor," 195.
[6] Dong, S., Haist, T. and Osten, W., "Hybrid wavefront sensor for the fast detection of wavefront disturbances," Appl. Opt. **51**(25), 6268 (2012).
[7] Dong, S., Haist, T., Dietrich, T. and Osten, W., "Hybrid curvature and modal wavefront sensor," presented at SPIE Optical Engineering + Applications, 18 September 2014, San Diego, California, United States, 922702.
[8] Guthery, C. E. and Hart, M., "Theory and Design of a Hybrid Wave-front Sensor for Adaptive Optics," Imaging and Applied Optics 2019 (COSI, IS, MATH, pcAOP), PTu3C.4, OSA, Munich (2019).
[9] Guthery, C. E. and Hart, M., "Pyramid and Shack–Hartmann hybrid wave-front sensor," Opt. Lett., OL **46**(5), 1045–1048 (2021).
[10] Pazder, J., Kooten, M., Lardière, O. and Véran, J.-P., "Double-Pyramid Wavefront Sensors: Tolerance Relaxation and Cheaper Alternatives using Achromatic Double-Roof Prisms," 1 January 2017.
[11] Hamilton, R. J., Rice, J. A., Guthery, C. E. and Hart, M., "Designing, Building, and Testing of a Hybrid Wavefront Sensor for Adaptive Optics," Imaging and Applied Optics 2019 (COSI, IS, MATH, pcAOP), JW2A.35, OSA, Munich (2019).